

1
2
3 **NADPH oxidase mediates microtubule alterations and diaphragm**
4 **dysfunction in dystrophic mice**
5
6
7
8
9

10
11 James A. Loehr¹, Shang Wang¹, Tanya R. Cully¹, Rituraj Pal¹, Irina V. Larina¹, Kirill V.
12 Larin^{1,2,3}, and George G. Rodney^{1*}
13

14 ¹Department of Molecular Physiology and Biophysics, Baylor College of Medicine, Houston,
15 TX, 77030, ²Department of Biomedical Engineering, University of Houston, Houston, TX,
16 77204, ³Interdisciplinary Laboratory of Biophotonics, Tomsk State University, Tomsk 634050,
17 Russia
18
19
20
21
22
23
24
25
26
27
28
29
30
31
32
33
34
35
36

37 ***Correspondence:**
38

39 Dr. George G. Rodney
40 Baylor College of Medicine
41 Department of Molecular Physiology & Biophysics
42 One Baylor Plaza-BCM335
43 Houston, TX, 77030, USA
44 713-798-5797
45 rodney@bcm.edu
46
47

48 **Keywords: optical coherence elastography, microtubule, fibrosis, stiffness,**

49 **Abstract**

50 Skeletal muscle from *mdx* mice is characterized by increased Nox2 ROS, altered microtubule
51 network, increased muscle stiffness, and decreased muscle/respiratory function. While
52 microtubule de-tyrosination has been suggested to increase stiffness and Nox2 ROS production
53 in isolated single myofibers, its role in altering tissue stiffness and muscle function has not been
54 established. Because Nox2 ROS production is upregulated prior to microtubule network
55 alterations and ROS affect microtubule formation, we investigated the role of Nox2 ROS in
56 diaphragm tissue microtubule organization, stiffness and muscle/respiratory function.
57 Eliminating Nox2 ROS prevents microtubule disorganization and reduces fibrosis and muscle
58 stiffness in *mdx* diaphragm. Fibrosis accounts for the majority of variance in diaphragm stiffness
59 and decreased function, implicating altered extracellular matrix and not microtubule de-
60 tyrosination as a modulator of diaphragm tissue function. Ultimately, inhibiting Nox2 ROS
61 production increased force and respiratory function in dystrophic diaphragm, establishing Nox2
62 as a potential therapeutic target in Duchenne muscular dystrophy.

63
64
65
66
67
68
69
70
71
72
73
74
75
76
77
78
79
80
81
82
83
84
85
86
87
88
89
90
91
92
93
94
95
96
97
98

99 **Introduction**

100 Duchenne muscular dystrophy (DMD) is an X-linked recessive disease which affects 1 in every
101 3500 boys resulting in progressive muscle atrophy, loss of ambulation and cardio-respiratory
102 failure (Levi, Genin, Angelini, Halevy, & Pines, 2015). In DMD patients, the leading cause of
103 mortality is diaphragm dysfunction (Finder et al., 2004; Finsterer & Stöllberger, 2003; Percival
104 et al., 2012). In the *mdx* animal, a mouse model of DMD, disease progression in the diaphragm
105 mimics the human development of the disease (Stedman et al., 1991), and respiratory
106 dysfunction has been shown to promote cardiac dysfunction (Barbin et al., 2016; Finder et al.,
107 2004; Lanza et al., 2001).

108
109 NADPH Oxidase 2 (Nox2) has been shown to play an important role in dystrophic muscle. Nox2
110 content and activity are upregulated prior to the onset of inflammation and necrosis (N.P.
111 Whitehead, Yeung, Froehner, & Allen, 2010) and downregulating Nox2 ROS production
112 protects against pathophysiological alterations in young (5-7 wk) dystrophic muscle (Pal et al.,
113 2014). Recent evidence indicates the microtubule (MT) network is dysregulated in dystrophic
114 muscle (Belanto et al., 2016; Iyer et al., 2017; Khairallah et al., 2012; Prins et al., 2009), which
115 results in aberrant Nox2 ROS production and implicates Nox2 ROS in altered
116 mechanotransduction (Khairallah et al., 2012). However, Nox2 ROS is upregulated early (19 d;
117 (N.P. Whitehead et al., 2010)), prior to changes in the MT network (Belanto et al., 2016; Iyer et
118 al., 2017; Khairallah et al., 2012; Prins et al., 2009), and oxidation has been shown to be a post-
119 translational modification of the MT network (Clark, Hagedorn, & Landino, 2014; Landino,
120 Moynihan, Todd, & Kennett, 2004; Wilson & Gonzalez-Billault, 2015). These findings raise the
121 question of whether Nox2 ROS initiates changes in the MT network.

122
123 In addition to increased Nox2 ROS production and alterations in the MT network, dystrophic
124 muscle is characterized by increased fibrosis and muscle stiffness (Christophe Cornu, Goubel, &
125 Fardeau, 1998; C. Cornu, Goubel, & Fardeau, 2001; Virgilio, Martin, Peirce, & Blemker, 2015).
126 The de-tyrosination of α -tubulin (DT-tubulin) has been proposed as a mechanism which prevents
127 the de-polymerization of the MT network, causing an increase in muscle stiffness and
128 dysfunction in isolated muscle cells (Kerr et al., 2015; Robison et al., 2016). However, Belanto
129 et al (Belanto et al., 2016) demonstrated increased muscle stiffness with no differences in relative
130 DT-tubulin amount between *mdx* and WT mice. MT formation also is sensitive to the
131 extracellular environment (Myers, Applegate, Danuser, Fischer, & Waterman, 2011; Andrew J.
132 Putnam, Cunningham, Pillemer, & Mooney, 2003; A. J. Putnam, Schultz, & Mooney, 2001) and
133 increased extracellular matrix (ECM) has been implicated in increased muscle stiffness and
134 decreased force production (Desguerre et al., 2009; Meyer & Lieber, 2011; Percival et al., 2012;
135 Rowe et al., 2010; Wood et al., 2014). Intriguingly, transgenic *mdx* mice expressing either a
136 nearly full length dystrophin (Dys ^{Δ 71-78}-*mdx*) or overexpressing utrophin (*Fiona*) suggest that
137 MT density and organization is independent of the level of MT de-tyrosination (Belanto et al.,
138 2014; Belanto et al., 2016). Taken together, the role of de-tyrosinated MTs in tissue stiffness and
139 disease pathogenesis in muscular dystrophy is unclear.

140
141 Skeletal muscle stiffness traditionally has been evaluated using either atomic force microscopy
142 (AFM; (Canato et al., 2010; Kerr et al., 2015; Mathur, Collinsworth, Reichert, Kraus, & Truskey,
143 2001; van Zwieten et al., 2013)) or the passive properties of muscle measured during stretch
144 (Chady H. Hakim & Duan, 2013; C. H. Hakim, Grange, & Duan, 2011; Lopez, Pardo, Cox, &
145 Boriek, 2008; Rowe et al., 2010). AFM evaluates single muscle fiber stiffness but does not
146 consider cell-cell interactions or the influence of the extra cellular matrix. While evaluating
147 stiffness through muscle passive properties considers the series and parallel elastic components
148 together it does not differentiate between the contributions of longitudinal (series) or transverse

149 (parallel) tissue stiffness within overall muscle stiffness. Optical coherence elastography (OCE)
150 recently has been developed as a unique method to noninvasively evaluate tissue stiffness (Larin
151 & Sampson, 2017; Wang & Larin, 2014; Wang et al., 2012; Wang et al., 2014). Here we utilize
152 OCE to evaluate the differences in longitudinal and transverse tissue stiffness in the diaphragm
153 of *mdx* mice. Previous data indicate *mdx* muscle is compromised in the transverse direction
154 (Kumar, Khandelwal, Malya, Reid, & Boriek, 2004; Ramaswamy et al., 2011). Therefore, OCE
155 may provide a unique method to differentiate pathological alterations in longitudinal and
156 transverse stiffness and their impact on muscle function.

157
158 Because the altered MT network and fibrosis develop later in the disease pathology, after Nox2
159 ROS production has been initiated, we hypothesized that genetically eliminating Nox2 ROS
160 production would prevent alterations to the MT network and reduce diaphragm stiffness thereby
161 improving muscle and respiratory function in adult *mdx* mice. We also hypothesized, at the tissue
162 level, stiffness would be greater in the transverse direction and fibrosis would be the major
163 determinant of tissue stiffness.

164

165 **Results**

166 **Genetic deletion of Nox2 ROS production prevents disorganization of the microtubule 167 network in dystrophic muscle**

168 Previous data have shown that tubulin content is upregulated in muscular dystrophy, and DT-
169 tubulin may influence MT stability (Kerr et al., 2015; Khairallah et al., 2012; Prins et al., 2009).
170 However, Belanto et al (Belanto et al., 2016) have suggested that the relative DT-tubulin level is
171 not elevated in *mdx* muscle. Our data confirm that α -, β -, and DT-tubulin are elevated with
172 muscular dystrophy and extend these findings to show that eliminating Nox2 ROS production in
173 *mdx* mice prevents the increase in all three forms of tubulin (Fig. 1B-D). Because DT-tubulin is
174 the de-tyrosinated form of α -tubulin, and both DT- and α -tubulin are elevated in *mdx* muscle, we
175 assessed the fraction of α -tubulin that is de-tyrosinated. We found that there is no difference in
176 the DT-/ α -tubulin ratio between groups (Fig. 1E), suggesting that the increase in DT-tubulin is
177 likely due to increased α -tubulin. Khairallah et al (Khairallah et al., 2012) demonstrated Nox2
178 ROS production is increased in response to a polymerized MT network. We found that Nox2
179 ROS production leads to increased MT disorganization (Fig 1G-H) and density (Fig 1I) in
180 dystrophic diaphragm muscle which was prevented by eliminating Nox2 ROS. These results
181 indicate that Nox2-generated ROS increases tubulin content, MT disorganization and MT
182 polymerization in dystrophic diaphragm muscle and questions the role of DT-tubulin in MT
183 stabilization or density.

184

185 **Genetic inhibition of Nox2 ROS decreases skeletal muscle fibrosis**

186 Increased fibrosis is a pathological hallmark of muscular dystrophy. In accordance with previous
187 studies, we observed increased diaphragm fibrosis in *mdx* compared with WT mice (Fig 2).
188 Eliminating Nox2 ROS in dystrophic muscle resulted in reduced collagen as measured by
189 Trichrome staining (Fig 2A), hydroxyproline content (Fig 2B), and western blot (Fig 2C) as well
190 as fibronectin content (Fig 2C). These data suggest that decreasing Nox2 ROS results in a
191 significant decrease in fibrosis in the *mdx* diaphragm.

192

193 **Muscle stiffness and stretch induced ROS are reduced in Nox2 deficient dystrophic muscle**

194 Microtubules have been shown to be sensitive to the extracellular environment (Myers et al.,
195 2011; Andrew J. Putnam et al., 2003; A. J. Putnam et al., 2001) and cell to cell (transverse)
196 interactions are critical in skeletal muscle force transduction (Passerieux, Rossignol, Letellier, &
197 Delage, 2007; Purslow & Trotter, 1994; Ramaswamy et al., 2011). We evaluated the role of
198 Nox2 ROS in diaphragm mechanical properties using two distinct methods; passive stretch to

199 evaluate the series and parallel elastic components together and optical coherence elastography
200 (OCE) to differentiate between the contributions of series (longitudinal stiffness) and parallel
201 (transverse stiffness) components within overall muscle tissue stiffness. Figure 3A and E
202 demonstrate the system design for both passive stretch and OCE, respectively, Figure 3F shows a
203 sample OCT image of the diaphragm and Figure 3-video 1 illustrates a sample wave propagation
204 taken during OCE. Passive stiffness while lengthening the diaphragm to 120% L_0 was increased
205 in *mdx* compared with WT mice, and eliminating Nox2 ROS resulted in reduced tissue stiffness
206 compared with *mdx* diaphragm (Fig 3B-C). Transverse and longitudinal stiffness, using OCE,
207 was increased in diaphragm of *mdx* mice compared with WT mice. Interestingly, eliminating
208 Nox2 ROS production reduced only longitudinal stiffness in *Ncf1^{-/-}::mdx* (designated as p47^(-/-)/*mdx*)
209 mice to WT levels (Fig. 3G-H). Muscle function was measured pre- and post-OCE to
210 ensure OCE measurements did not compromise tissue health. Muscle function for all genotypes
211 was not altered following OCE measurements (Fig. 3I). We also found that stretch induced ROS
212 was elevated in *mdx* diaphragm compared with both WT and p47^(-/-)/*mdx* diaphragm tissue (Fig
213 3D). These data suggest that elevated Nox2 ROS increases diaphragm stiffness in dystrophic
214 muscle and demonstrate Nox2 as the source of stretch induced ROS at the tissue level. In
215 addition, stiffness measured using OCE can detect changes in tissue elastic properties based on
216 fiber orientation and indicate a direction dependent response to alterations in tissue stiffness.

217

218 **Fibrosis is a major determinant of diaphragm stiffness**

219 Increased DT-tubulin has been suggested to stabilize the microtubule network resulting in less
220 dynamic microtubules thereby increasing tissue stiffness (Kerr et al., 2015; Robison et al., 2016).
221 Our results demonstrate that while both α - and DT-tubulin are upregulated in dystrophic muscle
222 the ratio of DT- to α -tubulin revealed no significant difference between groups (Fig. 1E). A
223 linear regression analysis demonstrated that fibrosis, DT-tubulin and α -tubulin significantly
224 correlate to transverse and longitudinal diaphragm stiffness while the DT-/ α -tubulin ratio only
225 demonstrated a significant correlation with longitudinal stiffness (Table 1). A multiple linear
226 regression analysis with either DT- or DT-/ α -tubulin ratio and fibrosis revealed that the variance
227 was no different than fibrosis alone (Table 1). Fibrosis accounted for 45% of the variance in the
228 longitudinal and nearly 70% in the transverse direction. These data indicate while tubulin content
229 correlates with muscle stiffness, fibrosis accounts for the majority of the variance in muscle
230 stiffness at the tissue level.

231

232

233 **Eliminating Nox2 ROS improves diaphragm muscle and respiratory function**

234 Diaphragm muscle and respiratory function are compromised in *mdx* mice (Huang et al., 2011;
235 Ishizaki et al., 2008; Pal et al., 2014; Percival et al., 2012). We previously have shown that
236 eliminating Nox2 ROS production protected against diaphragm alterations in young (4-6 wks)
237 *mdx* mice (Pal et al., 2014). Given muscle dysfunction in dystrophy is progressive, we wanted to
238 determine whether eliminating Nox2 ROS provided protection against muscle/diaphragm
239 dysfunction in older dystrophic mice. Here, we show that diaphragm function is impaired in
240 adult (16-24 wks) *mdx* muscle and eliminating Nox2 ROS partially protected against the force
241 deficits (Fig 4A). Eliminating Nox2 ROS in adult dystrophic muscle also protected against
242 alterations in diaphragm fiber cross sectional area, fiber type and central nuclei (Figure 4- S2).
243 These results, in combination with our previous data (Pal et al., 2014), indicate the lack of Nox2
244 ROS provides protection against pathophysiological alterations observed in dystrophic
245 diaphragm muscle at different stages of disease pathology. In addition, eliminating Nox2 ROS
246 protected against decrements in respiratory rate (f), minute ventilation (Mv), and peak inspiratory
247 flow (PIF) in adult *mdx* mice (Table 3). A linear regression analysis demonstrated that fibrosis
248 (Fig 4B) and both transverse and longitudinal diaphragm stiffness (Figure 4-figure supplement 2)

249 significantly correlated with peak diaphragm force. A multiple linear regression analysis
250 revealed when either transverse or longitudinal diaphragm stiffness was included with fibrosis,
251 the variance was no different than fibrosis alone (Table 2). These data indicate Nox2-derived
252 ROS drive alterations in *mdx* diaphragm which lead to diaphragm and respiratory dysfunction.

253

254

255 **Taxol induced MT polymerization has no effect on tissue stiffness but induced ROS** 256 **production**

257 To further elucidate the role of the MT network in tissue stiffness and ROS production, we
258 incubated WT diaphragm with Taxol to polymerize the MT network. We observed similar
259 alterations in the MT network between Taxol treated WT and *mdx* animals (Fig 1 F-I; Fig 5 A-
260 D). Taxol increased MT density (Fig 5D) and resulted in disorganization of the MT network (Fig
261 5B-C). There was no difference in passive stiffness between Taxol and DMSO treated diaphragm
262 tissue (Fig 5E-F); however, there was a difference in stretch induced ROS production (Fig 5G).
263 These data, in combination with our previous data, support the idea that while alterations in the
264 MT network increase ROS production, increases in DT-tubulin, MT density or MT
265 disorganization do not influence tissue stiffness.

266

267 **Discussion**

268 Froehner and colleagues (Percival et al., 2007) originally demonstrated MT disorganization in
269 dystrophic muscle and its subsequent restoration with the re-introduction of mini-dystrophin. In
270 *mdx* mice, the MT network becomes altered at approximately 7-8 wks of age (Prins et al., 2009)
271 and remains altered with age (9-11 months) (Kerr et al., 2015). It has been suggested that
272 alterations in the MT network lead to increased Nox2 ROS production and altered
273 mechanotransduction in adult *mdx* muscle (Kerr et al., 2015; Khairallah et al., 2012). However,
274 Nox2 ROS is upregulated prior to changes in the MT network (Kerr et al., 2015; Prins et al.,
275 2009; N.P. Whitehead et al., 2010), raising the question whether increased Nox2 ROS drives
276 changes in the MT network. In neurons, tubulin oxidation prevents MT polymerization (Clark et
277 al., 2014; Landino et al., 2004; Wilson & Gonzalez-Billault, 2015); however, it is unclear what
278 role increased ROS production plays in modulating the MT network of skeletal muscle. Our data
279 show that diaphragm MT alterations are increased in adult dystrophic muscle and eliminating
280 Nox2 ROS prevented the increase in α -, β -, and DT-tubulin content (Fig. 1B-D), MT density
281 (Fig. 1I), MT disorganization (Fig. 1G-H) and stiffness (Fig. 3C, G-H) observed in *mdx* mice.
282 The MT network can be affected by muscle fiber type and regeneration (Percival et al., 2007; E.
283 Ralston, Lu, & Ploug, 1999; Evelyn Ralston, Ploug, Kalhovde, & Lømo, 2001); both of which
284 are altered in dystrophic muscle. Here we show that eliminating Nox2 ROS protected against
285 alterations in fiber type switching and reduced central nuclei in dystrophic muscle. These data
286 indicate Nox2 ROS, either directly or indirectly through alterations in fiber type or regeneration
287 is modulating the MT network.

288

289 Previous work has focused on either the cortical (Percival et al.; Prins et al.) or some
290 undetermined combination of the cortical and intermyofibrillar MT network (Kerr et al.;
291 Khairallah et al.). However, given the intermyofibrillar MT network surrounds the contractile
292 apparatus, any alterations to this network likely affect force production. In addition, Nox2 is
293 located in the plasma membrane and 60-90% of the plasma membrane in skeletal muscle is
294 comprised by the t-tubules (Eisenberg & Kuda; Mobley & Eisenberg; Peachey, 1965).
295 Therefore, the intermyofibrillar MT network may contribute more to muscle function and the
296 mechanical activation of Nox2 ROS compared with the cortical MT network. To further explore
297 whether the altered intermyofibrillar MT network influenced diaphragm stiffness and ROS

298 production we incubated WT diaphragm with Taxol. Polymerizing the MT network with Taxol
299 resulted in increased intermyofibrillar MT density (Fig. 5D) and disorganization (Fig. 5B-C),
300 similar to the diaphragm from *mdx* mice, but no change in tissue stiffness was detected. We
301 found that Taxol increased stretch dependent ROS production at the tissue level (Fig. 5F);
302 similar to what Khairallah et al has shown in single FDB fibers (Khairallah et al., 2012). Taken
303 together, we show that Nox2 ROS is an early event that modulates the MT network, potentially
304 resulting in a feed forward mechanism where elevated Nox2 ROS production increases MT
305 density and disorganization which in turn leads to additional Nox2 ROS production. We
306 currently are investigating the mechanisms by which Nox2 ROS modulates the MT network.

307
308 Respiratory insufficiency in the DMD patient is caused by respiratory muscle weakness, leading
309 to impaired ventilation through an inability to inhale and exhale fully, ultimately resulting in a
310 need for mechanical ventilation. Dystrophic muscle is characterized by increased fibrosis and
311 while some show no link between altered collagen and stiffness (Chapman, Pichika, & Lieber,
312 2015; Smith & Barton, 2014) others have implicated fibrosis in decreased function and stiffness
313 (Cabrera et al., 2014; Desguerre et al., 2009; Ishizaki et al., 2008; Mead et al., 2014; Meyer &
314 Lieber, 2011; Percival et al., 2012; Rowe et al., 2010; Wood et al., 2014). Lateral force
315 transmission through the endomysial layer of skeletal muscle has been shown to be important in
316 overall force production (Passerieux et al., 2007; Patel & Lieber, 1997; Purslow & Trotter, 1994;
317 Trotter & Purslow, 1992) and, in *mdx* mice, force is compromised in the transverse direction
318 (Kumar et al., 2004; Ramaswamy et al., 2011). The endomysial layer also has increased levels of
319 fibrosis which affects force production and correlates with the age of loss of ambulation in
320 dystrophic muscle (Desguerre et al., 2012; Desguerre et al., 2009). Here we show decreased
321 diaphragm muscle (Fig 4A) and respiratory function (Table 3) and increased fibrosis (Fig 2B)
322 and tissue stiffness (Fig. 3 C, G-H) in dystrophic muscle. Eliminating Nox2 ROS in dystrophic
323 diaphragm muscle reduced fibrosis and tissue stiffness, increased force and prevented the decline
324 in respiratory function. Highlighting the importance of cell-cell interactions, our data
325 demonstrate a stronger correlation between force and transverse stiffness (Fig S3) and fibrosis
326 and transverse stiffness than longitudinal stiffness (Table 1). These data indicate that fibrosis is a
327 crucial factor altering tissue stiffness and force production resulting in impaired cell-cell
328 interactions. Furthermore, a 26% increase in diaphragm force maintained respiratory function in
329 the *p47^{-/-}/mdx* mouse, likely decreasing the need to place patients on a ventilator.

330
331 Several therapeutics designed to reduce fibrosis have proved beneficial in improving muscle
332 function in dystrophic muscle (Cabrera et al., 2014; Huebner, Jassal, Halevy, Pines, & Anderson,
333 2008; Percival et al., 2012; Turgeman et al., 2008; N. P. Whitehead, Kim, Bible, Adams, &
334 Froehner, 2015). Therefore, based on our data, it is conceivable that decreased fibrosis reduces
335 transverse muscle stiffness, improving lateral force transmission and thereby overall muscle
336 function. In addition, it has been suggested that fibrosis induces a feed forward loop causing
337 collagen producing myogenic cells not to differentiate into terminal satellite cells; inhibiting
338 myogenesis and enhancing fibrosis (Alexakis, Partridge, & Bou-Gharios, 2007). These data are
339 supported by the idea that progenitor cells take on a fibrogenic-like phenotype with aging;
340 resulting in the loss of regenerative capacity in dystrophic muscle (Biressi, Miyabara, Gopinath,
341 Carlig, & Rando, 2014; Pessina et al., 2015). The reduction in fibrosis observed by eliminating
342 Nox2 ROS in dystrophic muscle may implicate a role for improved satellite cell activity given
343 the reduced central nuclei (Fig S2C) and the increased CSA (Fig S2A) and Type 2B fibers (Fig
344 S2E) observed in the *p47^{-/-}/mdx* mice. In addition, we previously demonstrated eliminating Nox2
345 ROS improves autophagy in dystrophic muscle (Pal et al., 2014) and autophagy is necessary for

346 satellite cell differentiation and fusion (Fortini et al., 2016). Future experiments are needed to
347 investigate the role of Nox2 ROS in the impairment of satellite cell function

348
349 Tissue stiffness in leg muscle mirrors changes in the MT network; becoming altered in *mdx*
350 animals at approximately 7-8 wks of age (Wolff et al., 2006) and remaining elevated in older
351 animals (C. H. Hakim et al., 2011). Skeletal muscle stiffness has predominantly been assessed
352 using atomic force microscopy (AFM) on single fibers (Canato et al., 2010; Kerr et al., 2015;
353 Mathur et al., 2001; van Zwieten et al., 2013) or by passively lengthening muscle tissue (Chady
354 H. Hakim & Duan, 2013; C. H. Hakim et al., 2011; Lopez et al., 2008; Rowe et al., 2010). In
355 C2C12 cells and isolated adult myofibers, alterations to the MT network increased cell stiffness,
356 measured via AFM, and altered mechanotransduction (Kerr et al., 2015; Khairallah et al., 2012).
357 However, AFM uses a point specific bending moment evaluating only the near-membrane
358 mechanical properties at that point (Kerr et al., 2015). While this approach is vital for
359 understanding intracellular contributions to single cell signaling and near-membrane mechanics,
360 it does not consider the ECM or cell-cell interactions in overall tissue mechanotransduction.
361 Passive stretch takes into consideration both of these factors; however, it evaluates both the
362 series (longitudinal) and parallel (transverse) elastic components together, making it difficult to
363 assess the individual contributions to overall tissue stiffness. To address these limitations, we
364 used two techniques to evaluate tissue stiffness, passive stretch and OCE. Interestingly,
365 eliminating Nox2 ROS production partially prevented increases in tissue stiffness during passive
366 lengthening (Fig 3C) similar to transverse stiffness measured using OCE (Fig 3G). In addition,
367 we demonstrate a partial protection against force decrement (Fig 4A) and elevated transverse
368 stiffness by eliminating Nox2 ROS production in the diaphragm (Fig 3G). These data highlight
369 the importance of lateral (transverse) force transmission, and the significance of transverse
370 stiffness in force production.

371
372 In isolated muscle cells, DT-tubulin, the de-tyrosinated form of α -tubulin, has been suggested to
373 stabilize the MT network resulting in increased stiffness and reduced force (Kerr et al., 2015;
374 Robison et al., 2016). However, MT formation is sensitive to alterations in the extracellular
375 environment (Myers et al., 2011; Andrew J. Putnam et al., 2003; A. J. Putnam et al., 2001)
376 implicating fibrosis in altering tissue stiffness. Previous work in neurons (Bartolini et al., 2016;
377 Cook, Nagasaki, & Gundersen, 1998; Infante, Stein, Zhai, Borisy, & Gundersen, 2000; Khawaja,
378 Gundersen, & Bulinski, 1988; Morris, Nader, Ramalingam, Bartolini, & Gundersen, 2014;
379 Skoufias & Wilson, 1998; Webster, Wehland, Weber, & Borisy, 1990) indicates DT-tubulin
380 simply occurs temporally at the same time but was not the cause of MT stabilization and in
381 skeletal muscle, Belanto et al (Belanto et al., 2016) recently demonstrated while DT-tubulin was
382 elevated in *mdx* quadriceps muscle, the fraction of DT-/ α -tubulin was no different than WT mice.
383 Our data support the idea that while DT-tubulin is elevated in dystrophic diaphragm the DT-/ α -
384 tubulin ratio is no different (Fig 1E), indicating elevated DT-tubulin is a function of elevated α -
385 tubulin and not the cause of stabilized MTs. Using the DT-/ α -tubulin ratio as the indicator of
386 stabilized MTs, our data demonstrate a significant but weak correlation with OCE longitudinal
387 diaphragm stiffness and no correlation with transverse stiffness (Table 1). When included with
388 fibrosis, while elevated DT-tubulin and the DT-/ α -tubulin ratio correlated with tissue stiffness,
389 MLR revealed neither influenced diaphragm tissue stiffness above fibrosis. These data suggest
390 neither the absolute nor the relative amount of DT-tubulin influence tissue stiffness and fibrosis
391 is the main determinant of diaphragm tissue stiffness.

392
393 Nox2 protein level and ROS production are upregulated early in dystrophic muscle prior to the
394 inflammatory response (Pal et al., 2014; N.P. Whitehead et al., 2010). Previously, we have
395 shown that Nox2 ROS production initiates a feed forward loop exacerbating Nox2 ROS

396 production and inhibiting autophagic flux through activation of Src kinase (Pal et al., 2014).
397 Interestingly, recent data by Froehner and colleagues (N. P. Whitehead, Kim, Bible, Adams, &
398 Froehner, 2015) have shown that simvastatin reduced Nox2 protein levels, oxidative stress and
399 fibrosis in *mdx* mice. Here we provide evidence for an additional feedforward mechanism where
400 Nox2 ROS alters the MT network, which in turn exacerbates Nox2 ROS production. We also
401 demonstrate that eliminating Nox2 ROS production alleviates many of the pathophysiological
402 alterations, such as fibrosis, which occur in dystrophic diaphragm muscle. Taken together, there
403 is compelling evidence that Nox2 ROS production is a central event in exacerbating disease
404 pathology, implicating Nox2 as a viable therapeutic target in muscular dystrophy.

405

406 **Materials and Methods**

407 **Animals**

408 C57Bl/6J (WT) and C57Bl/10ScSn-Dmdmdx/J (*mdx*) were purchased from Jackson Laboratories
409 (Bar Harbor, ME) and bred following their breeding strategy. Mice lacking p47^{phox} (B6(Cg)-
410 Ncf1m1J/J, JaxMice) were crossed with *mdx* mice to generate *Ncf1^{-/-}::mdx* (p47^(-/-)/*mdx*) mice
411 (Pal et al., 2014)). At approximately 5 months of age and in accordance with National Institutes
412 of Health guidelines and approved by the Institutional Animal Care and Use Committee of
413 Baylor College of Medicine, mice were anesthetized by isoflurane (2%) inhalation and
414 euthanized by rapid cervical dislocation followed by thoracotomy.

415

416 **Diaphragm passive stretch**

417 Diaphragm muscle was surgically dissected and sectioned into diaphragm strips with the rib end
418 attached to a fixed hook and the other to the lever arm of a dual-mode lever system (305C-LR-
419 FP; Aurora Scientific Inc., Aurora, ON, Canada) using silk suture (4-0). The diaphragm was
420 placed in a physiological saline solution containing (in mM): 2.0 CaCl₂, 120.0 NaCl, 4.0 KCl,
421 1.0 MgSO₄, 25.0 NaHCO₃, 1.0 KH₂PO₄, 10.0 glucose, pH 7.3 and continuously gassed with
422 95% O₂-5% CO₂ at 25 °C. Muscle length was adjusted to elicit maximum twitch force (optimal
423 length, L_o). A hand-held electronic caliper was used to measure L_o and the lever arm was
424 programmed to passively stretch the diaphragm strip to 120% of L_o at 1 L_o/s for 5 min. At the
425 end of the stretch protocol fiber bundles were removed from the rib, trimmed of excess
426 connective tissue, blotted dry, and weighed. Muscle weight and L_o were used to estimate
427 absolute forces expressed as N/cm² (Close, 1972).

428

429 To determine tissue stiffness, the Veronda-Westman model (Veronda & Westmann, 1970) was
430 employed to quantify Young's modulus for the first stretch. The Veronda-Westman model
431 describes a nonlinear relationship between stress and strain and previously has been utilized to
432 study the elasticity of a number of biological tissues, such as breast and skin (Krouskop,
433 Wheeler, Kallel, Garra, & Hall, 1998; Veronda & Westmann, 1970). Assuming the diaphragm
434 tissue as an incompressible Veronda-Westman material, under uniaxial tension, the axial stress σ
435 is related to the resulted stretch λ through equation 1: (Oberai et al., 2009; Pavan, Madsen,
436 Frank, Adilton, & Hall, 2010)

437

$$438 \quad \sigma = \frac{2E}{3} \left(\lambda^2 - \frac{1}{\lambda} \right) \left(e^{\gamma(\lambda^2 + \frac{2}{\lambda} - 3)} - \frac{1}{2\lambda} \right), \quad \text{Eq. 1}$$

439

440

441 where $\lambda = 1 + \varepsilon$ (ε is the strain), E is the Young's modulus of the diaphragm tissue at zero strain
442 and γ is a nonlinear parameter representing the exponential increase rate of the Young's modulus
443 over the increase of strain. Young's modulus was calculated through fitting the experimental data
444 with Eq. 1 in Matlab (MathWorks; Natick, MA).

445

446 **ROS Measurements**

447 Diaphragm intracellular ROS was measured using 6-carboxy-2',7'-dichlorodihydrofluorescein
448 diacetate (DCFH-DA) (Invitrogen, Carlsbad, CA). Prior to stretch, the diaphragm was incubated
449 with DCFH-DA for 30 min, washed using the physiological saline solution and de-esterified for
450 an additional 30 min at 25°C. All cell-loading and imaging was performed in the dark to prevent
451 light induced oxidation of DCFH-DA. A Sutter Lamda DG-5 Ultra high-speed wavelength
452 switcher was used to excite DCF at 470/20 nm and emission intensity was collected at 535/48
453 nm on a charge coupled device (CCD) Camera (CoolSNAP MYO, Photometrics, Tucson, AZ)
454 attached to an Axio Observer (Zeiss) inverted microscope (20× objective, 0.5 NA) at a rate of 0.2
455 Hz. Alterations in the rate of ROS production were baseline corrected and calculated over the
456 final minute of the stretch period.

457

458 **Effect of Taxol on Tissue Stiffness and ROS Production**

459 WT diaphragm tissue was incubated with 20 μM Taxol (Sigma-Aldrich, St. Louis, MO) or
460 DMSO (Sigma-Aldrich, St. Louis, MO) control for 2 hr at RT. After 1 hr the tissue was
461 incubated with DCFH-DA, de-esterified and passively stretched as described above.

462

463 **Optical coherence elastography**

464 Optical coherence elastography (OCE) is a novel technique for nondestructive assessment of mechanical
465 properties of tissues (Kennedy, Wijesinghe, & Sampson, 2017; Larin & Sampson, 2017). The
466 principle of OCE is based on producing a pressure wave on the sample and monitoring the propagation of
467 the wave using phase-sensitive optical coherence tomography (OCT) imaging on nanometer scale. The
468 velocity of the wave propagation in different directions along the surface is used to deduct tissue elasticity
469 anisotropically (Li, Guan, Huang, Johnstone, & Wang, 2012; Wang et al., 2012). A home-built
470 OCE system was utilized which contains a focused air-puff device for tissue stimulation (Wang
471 et al., 2013) and a spectral-domain OCT system to capture the tissue mechanical response (Wang
472 et al., 2014). The air-puff system provided a highly-localized (~150 μm in diameter), short-
473 duration (~1 ms), and low-pressure (below 10 Pa) air stream to stimulate the surface of the
474 diaphragm tissue in a noncontact fashion. The induced tissue displacement had a micro-scale
475 amplitude. The OCT system had an axial resolution of ~5 μm in tissue, an imaging beam
476 diameter of ~4 μm at the focal plane, and a displacement sensitivity of ~11 nm with the phase of
477 the OCT complex signal. The tissue displacement over time was detected using the temporal
478 phase profile from the OCT system. A previously reported shear wave imaging OCT approach
479 (Wang & Larin) was utilized to capture the elastic wave propagation in a depth-resolved 2D field
480 of view with a time resolution of 16 μs. Cross-correlation of tissue displacement profiles was
481 used to measure the time delay formed by the wave propagation at different locations. The elastic
482 wave velocity was thus quantified based on the slope from a linear fit of the time delay with
483 respect to the wave propagation distance. A surface wave model (Doyle, 1997) that relates the
484 sample Young's modulus E to the wave velocity C was utilized to estimate the tissue elasticity
485 through equation 2: (Li et al., 2012; Wang et al., 2012)

486

487

$$E = \frac{2\rho \times (1+\nu)^3 \times C^2}{(0.87+1.12\nu)^2} \quad \text{Eq. 2}$$

488

489 where ρ is the tissue density and ν is the Poisson's ratio; diaphragm density was 1060 kg/m³
490 (Mendez & Keys, 1960). Due to the nearly incompressibility of soft tissue, the Poisson's ratio of
491 0.5 was utilized (Mathur et al., 2001). The averaged wave velocity value from 0-0.1 mm depth
492 range from the tissue surface was used for calculation of the Young's modulus. For each

493 diaphragm sample, the elastic wave assessment was conducted in the transverse and longitudinal
494 directions of the muscle fiber.

495

496 ***Ex vivo* force measurements**

497 Diaphragm muscle was surgically dissected from mice and sectioned into diaphragm strips with
498 one end attached to a fixed hook and the other to a force transducer (F30, Harvard Apparatus)
499 using silk suture (4-0) in a physiological saline solution continuously gassed with 95% O₂–5%
500 CO₂ at 25°C. Diaphragm strips were incubated at 25°C for 10 min and optimal muscle length
501 (L_o) and voltage (V_{max}) were adjusted to elicit maximum twitch force. Following a 5 min rest
502 period, the diaphragm strip was stimulated at 150 Hz with pulse and train durations of 0.5 and
503 250 ms, respectively. Immediately after stimulation, L_o was determined using a hand-held
504 electronic caliper and the diaphragm strip was placed at L_o in a 100 x 15 mm petri dish (VWR,
505 Radnor, PA) for OCE measurements. Following OCE, the diaphragm was re-suspended from the
506 force transducer at L_o and after a 5 min rest period stimulated again at 150 Hz to ensure OCE
507 measurements did not compromise the diaphragms functional properties.

508

509 To determine the force-frequency relationship, diaphragm strips were incubated at 30°C for 15
510 min and L_o and V_{max} were adjusted to elicit maximum twitch force. Following a 5 min rest
511 period, force-frequency characteristics were measured at stimulation frequencies of 1, 5, 10, 20,
512 40, 60, 80, and 100-Hz every minute with pulse and train durations of 0.5 and 250 ms. At the end
513 of the contractile protocol L_o was measured using a hand-held electronic caliper. Following both
514 stimulation protocols, fiber bundles were trimmed of excess bone and connective tissue, blotted
515 dry, and weighed. Muscle weight and L_o were used to estimate cross-sectional area and absolute
516 forces expressed as N/cm² (Close).

517

518 **Unrestrained whole-body plethysmography**

519 Respiratory function was monitored in unrestrained mice using Buxco small animal whole-body
520 plethysmography (Data Sciences International, New Brighton, MN) and FinePointe software
521 (Data Sciences International, New Brighton, MN). The system was calibrated each day prior to
522 data collection. On the day of data collection, animals were placed in individual chambers and
523 given 30 min to acclimate; followed by 60 min of data collection. The software averaged the data
524 over each minute and recorded a value every minute for 60 min. To ensure data was
525 representative, breath frequency was used to ensure the mouse had not held its breath, buried its
526 head under its body or was breathing too rapidly. Mean breath frequency was calculated and data
527 which fell outside 1SD of the mean was excluded from the data analysis (Roberts, Holley-
528 Cuthrell, Gonzalez-Vega, Mull, & Heydemann, 2015).

529

530 **Western Blot**

531 Lysates from diaphragm tissue were extracted and quantified with the bicinchoninic acid (BCA)
532 protein assay kit (Pierce, Rockford, IL), using BSA as the standard. Lysates were separated via
533 SDS-PAGE and transferred to polyvinylidene difluoride (PVDF) membranes. All tubulin blots were
534 incubated in blocking buffer (5%, w/v, dried skimmed milk in Tris-buffered saline, pH 7.4, and
535 0.2% Tween 20; TBST) for 60 min and incubated overnight with anti- α -tubulin (Santa Cruz
536 Biotechnologies), anti- β -tubulin (Cell Signaling Technology), anti-detyrosinated tubulin
537 (Millipore) and anti-GAPDH (Millipore) in blocking buffer. Fibronectin and collagen blots were
538 blocked for 60 min in blocking buffer as above except with .05% Tween 20 and incubated with
539 anti-fibronectin (Millipore), anti-collagen (Abcam) and anti-GAPDH for 60 min at room
540 temperature (RT). Tubulin and fibronectin blots were exposed to IRDye® Secondary Antibodies
541 (LI-COR Biosciences) diluted in TBST for 60 min at RT and washed again. The LI-COR®
542 Odyssey Infrared Imaging System was used for blot detection and ImageJ software for blot

543 analysis. The collagen blot was probed with secondary antibodies; ECL anti-mouse IgG HRP
544 (NA931, GE Healthcare) and ECL Anti-rabbit IgG HRP (NA93401, GE Healthcare) for 60 min
545 at RT. The membrane was imaged using the Chemidoc touch with Clarity and Clarity Max ECL
546 reagent (Bio-Rad, Hercules, CA). Image analysis was performed using Biorad Image Lab 6.0
547 software.

548

549 **Hydroxyproline Assay**

550 Diaphragm collagen content was measured using a hydroxyproline assay kit (Sigma-Aldrich, St.
551 Louis, MO). Briefly, diaphragm tissue was homogenized and hydrolyzed in 200 μ l of 6 M
552 hydrochloric acid at 100 °C for 3 hours. Hydrolysate was transferred to a 96-well plate (Corning,
553 Corning, NY) and evaporated in an oven at 60 °C. Following evaporation, the Chloramine
554 T/Oxidation Buffer mixture was added to all wells and incubated for 5 min at RT. DMAB (4-
555 (Dimethylamino) benzaldehyde) was diluted in a Perchloric Acid/Isopropanol solution, added to
556 all wells, and incubated for 90 min at 60 °C. A hydroxyproline standard curve (0-1.0 μ g) was
557 included in the assay to quantify hydroxyproline content in each sample. All samples, including
558 the standard curve, were performed in duplicate and absorbance was measured at 560 nm.
559 Results are reported as μ g of hydroxyproline per mg of tissue (μ g/mg).

560

561 **Immunofluorescence**

562 For fiber-type, serial diaphragm sections of 12-14 μ m thickness were sectioned at -24°C using a
563 refrigerated cryostat (Shandon Cryotome E, Thermo). Sections were fixed with cold methanol
564 for 20 min and incubated overnight in a humid box at 4°C with Anti-Type I (BA-F8) and anti-
565 Type IIA (SC-71) antibodies purchased from Developmental Studies Hybridoma Bank (DSHB;
566 Iowa City, IA). Sections were then incubated for 3 hours with IgG1 and IgG2b isotype-specific
567 secondary antibodies (Invitrogen, Waltham, MA). Slides were mounted with VECTASHIELD
568 anti-fade mounting media containing DAPI (Vector Laboratories, Berlingame, CA). Images were
569 acquired using a CCD camera (Digital Sight DS-Fi1, Nikon) attached to an upright microscope
570 (Nikon Eclipse 80i, 10 \times objective, 0.45 NA). Images were analyzed using ImageJ software.

571

572 For α -tubulin staining, diaphragm tissue was fixed at L₀ using 10% neutral buffered formalin
573 (VWR, Radnor, PA) for 2h at room temperature. The tissue was rinsed 3 times and stored in PBS
574 (ThermoScientific, Waltham, MA) plus 1 mM EDTA (Invitrogen, Waltham, MA). Diaphragm
575 fibers were mechanically dissociated from the fixed diaphragm strip into single fibers and placed
576 in 35 mm glass bottom culture dishes (MatTek, Ashland, MA) containing PBS plus 1 mM
577 EDTA. Fibers were permeabilized with 0.1% Triton X-100 in PBS plus 1 mM EDTA for 10 min.
578 After rinsing three times with PBS plus 1 mM EDTA, a blocking agent was added (0.1%
579 saponin, 10% FBS in PBS plus 1 mM EDTA) for 1 h at RT. Fibers were incubated with an
580 Alexa-Fluor 488 conjugated α -tubulin antibody (Life Technologies, Waltham, MA) for 2 d at 4
581 °C. Diaphragm fibers were washed with PBS and mounted with VECTASHIELD anti- fade
582 mounting media containing DAPI (Vector Laboratories, Berlingame, CA) prior to microscopy.
583 Fibers were imaged using a Zeiss LSM 780 confocal microscope (Zeiss, Oberkochen, Germany).
584 Microtubule organization was analyzed using custom software (Liu & Ralston, 2014) and
585 microtubule density was assessed by summing 10 images from the intra-myofibrillar region of
586 each fiber (> 3 μ m from surface), converted to a binary image and quantified using ImageJ
587 software. Images were subjected to background subtraction and contrast enhancement using
588 Image J for figure presentation only.

589

590 **Histology**

591 Using a refrigerated cryostat (Shandon Cryotome E, Thermo), 12-14 μ m thick serial sections
592 were cut from the mid-belly region of the diaphragm at -24°C. Sections were stained using

593 Masson's Trichrome for fibrosis and Hematoxylin and Eosin for cross sectional area (CSA) and
594 centralized nuclei. Images were acquired using a CCD camera (Digital Sight DS-Fi1, Nikon)
595 attached to an upright microscope (Nikon Eclipse 80i, 10× objective, 0.45 NA). Images were
596 analyzed using ImageJ software.

597

598 **Statistical Analysis**

599 Data are reported as mean ± SEM, unless otherwise specified. A 1-way ANOVA was used to
600 measure statistical differences between groups. A 2-way RM ANOVA was used to determine
601 statistical differences between groups for the force-frequency data. For CSA, a Kruskal-Wallis
602 ANOVA was used to determine differences between groups. Tukey's post-hoc test was used
603 when statistical differences were identified. Linear regression and multiple linear regression
604 models were used to determine correlations between variables. Statistical analysis was performed
605 in Origin Pro (OriginLab Corporation, Northampton, MA) with significance set *a priori* at $p \leq$
606 0.05.

607

608 **Acknowledgement**

609 The authors would like to thank Drs. Wenhua Liu and Evelyn Ralston (National Institute of
610 Arthritis and Musculoskeletal and Skin Diseases) for providing the directionality analysis
611 program. Research reported in this publication was supported by the National Institute of
612 Arthritis and Musculoskeletal and Skin Diseases of the National Institutes of Health under
613 Award Number R01 AR061370 to G.G.R., the National Heart, Lung, and Blood Institute of the
614 National Institutes of Health under Award Number R01 HL120140 to K.V.L. and I.V.L. and
615 T32 HL007676 to J.A.L. Additional support was provided by the National Eye Institute of the
616 National Institutes of Health under Award Number R01 EY022362 to K.V.L., the American
617 Heart Association under Award Number 16POST30990070 to S.W., and a Gillson Longenbaugh
618 Foundation Award to G.G.R.

619

620 **Competing Interests**

621 The authors have no financial or non-financial competing interests to disclose.

622

623 **References**

624

- 625 Alexakis, C., Partridge, T., & Bou-Gharios, G. (2007). Implication of the satellite cell in dystrophic muscle
626 fibrosis: a self-perpetuating mechanism of collagen overproduction. *Am J Physiol Cell Physiol*,
627 293(2), C661-669. doi:10.1152/ajpcell.00061.2007
- 628 Barbin, I. C., Pereira, J. A., Bersan Rovere, M., de Oliveira Moreira, D., Marques, M. J., & Santo Neto, H.
629 (2016). Diaphragm degeneration and cardiac structure in mdx mouse: potential clinical
630 implications for Duchenne muscular dystrophy. *J Anat*, 228(5), 784-791. doi:10.1111/joa.12443
- 631 Bartolini, F., Andres-Delgado, L., Qu, X., Nik, S., Ramalingam, N., Kremer, L., . . . Gundersen, G. G. (2016).
632 An mDia1-INT2 formin activation cascade facilitated by IQGAP1 regulates stable microtubules in
633 migrating cells. *Mol Biol Cell*, 27(11), 1797-1808. doi:10.1091/mbc.E15-07-0489
- 634 Belanto, J. J., Mader, T. L., Eckhoff, M. D., Strandjord, D. M., Banks, G. B., Gardner, M. K., . . . Ervasti, J.
635 M. (2014). Microtubule binding distinguishes dystrophin from utrophin. *Proc Natl Acad Sci U S A*,
636 111(15), 5723-5728. doi:10.1073/pnas.1323842111
- 637 Belanto, J. J., Olthoff, J. T., Mader, T. L., Chamberlain, C. M., Nelson, D. M., McCourt, P. M., . . . Ervasti, J.
638 M. (2016). Independent variability of microtubule perturbations associated with
639 dystrophinopathy. *Hum Mol Genet*, 25(22), 4951-4961. doi:10.1093/hmg/ddw318
- 640 Biressi, S., Miyabara, E. H., Gopinath, S. D., Carlig, P. M., & Rando, T. A. (2014). A Wnt-TGFbeta2 axis
641 induces a fibrogenic program in muscle stem cells from dystrophic mice. *Sci Transl Med*, 6(267),
642 267ra176. doi:10.1126/scitranslmed.3008411

643 Cabrera, D., Gutiérrez, J., Cabello-Verrugio, C., Morales, M. G., Mezzano, S., Fadic, R., . . . Brandan, E.
644 (2014). Andrographolide attenuates skeletal muscle dystrophy in mdx mice and increases
645 efficiency of cell therapy by reducing fibrosis. *Skeletal Muscle*, 4, 6-6. doi:10.1186/2044-5040-4-
646 6

647 Canato, M., Dal Maschio, M., Sbrana, F., Raiteri, R., Reggiani, C., Vassanelli, S., & Megighian, A. (2010).
648 Mechanical and Electrophysiological Properties of the Sarcolemma of Muscle Fibers in Two
649 Murine Models of Muscle Dystrophy: Col6a1^{-/-} and Mdx. *Journal of Biomedicine and*
650 *Biotechnology*, 2010, 981945. doi:10.1155/2010/981945

651 Chapman, M. A., Pichika, R., & Lieber, R. L. (2015). Collagen crosslinking does not dictate stiffness in a
652 transgenic mouse model of skeletal muscle fibrosis. *J Biomech*, 48(2), 375-378.
653 doi:10.1016/j.jbiomech.2014.12.005

654 Clark, H. M., Hagedorn, T. D., & Landino, L. M. (2014). Hypothiocyanous acid oxidation of tubulin
655 cysteines inhibits microtubule polymerization. *Archives of biochemistry and biophysics*, 541,
656 10.1016/j.abb.2013.10.1026. doi:10.1016/j.abb.2013.10.026

657 Close, R. I. (1972). Dynamic properties of mammalian skeletal muscles. *Physiol Rev.*, 52(1), 129-197.

658 Cook, T. A., Nagasaki, T., & Gundersen, G. G. (1998). Rho guanosine triphosphatase mediates the
659 selective stabilization of microtubules induced by lysophosphatidic acid. *J Cell Biol*, 141(1), 175-
660 185.

661 Cornu, C., Goubel, F., & Fardeau, M. (1998). Stiffness of knee extensors in Duchenne Muscular
662 Dystrophy. *Muscle & Nerve*, 21(12), 1772-1774. doi:10.1002/(SICI)1097-
663 4598(199812)21:12<1772::AID-MUS21>3.0.CO;2-0

664 Cornu, C., Goubel, F., & Fardeau, M. (2001). Muscle and joint elastic properties during elbow flexion in
665 Duchenne muscular dystrophy. *J Physiol*, 533(Pt 2), 605-616.

666 Desguerre, I., Arnold, L., Vignaud, A., Cuvellier, S., Yacoub-Youssef, H., Gherardi, R. K., . . . Chazaud, B.
667 (2012). A new model of experimental fibrosis in hindlimb skeletal muscle of adult mdx mouse
668 mimicking muscular dystrophy. *Muscle Nerve*, 45(6), 803-814. doi:10.1002/mus.23341

669 Desguerre, I., Mayer, M., Leturcq, F., Barbet, J. P., Gherardi, R. K., & Christov, C. (2009). Endomysial
670 fibrosis in Duchenne muscular dystrophy: a marker of poor outcome associated with
671 macrophage alternative activation. *J Neuropathol Exp Neurol*, 68(7), 762-773.
672 doi:10.1097/NEN.0b013e3181aa31c2

673 Doyle, J. F. (1997). *Wave propagation in structure: spectral analysis using fast discrete Fourier*
674 *transforms*.

675 Eisenberg, B. R., & Kuda, A. M. (1975). Stereological analysis of mammalian skeletal muscle. II. White
676 vastus muscle of the adult guinea pig. *J Ultrastruct Res*, 51(2), 176-187.

677 Finder, J. D., Birnkrant, D., Carl, J., Farber, H. J., Gozal, D., Iannaccone, S. T., . . . American Thoracic, S.
678 (2004). Respiratory care of the patient with Duchenne muscular dystrophy: ATS consensus
679 statement. *Am J Respir Crit Care Med*, 170(4), 456-465. doi:10.1164/rccm.200307-885ST

680 Finsterer, J., & Stöllberger, C. (2003). The Heart in Human Dystrophinopathies. *Cardiology*, 99(1), 1-19.
681 doi:10.1159/000068446

682 Fortini, P., Ferretti, C., Iorio, E., Cagnin, M., Garribba, L., Pietraforte, D., . . . Dogliotti, E. (2016). The fine
683 tuning of metabolism, autophagy and differentiation during in vitro myogenesis. *Cell Death Dis*,
684 7, e2168. doi:10.1038/cddis.2016.50

685 Hakim, C. H., & Duan, D. (2013). Truncated dystrophins reduce muscle stiffness in the extensor
686 digitorum longus muscle of mdx mice. *Journal of Applied Physiology*, 114(4), 482-489.
687 doi:10.1152/jappphysiol.00866.2012

688 Hakim, C. H., Grange, R. W., & Duan, D. (2011). The passive mechanical properties of the extensor
689 digitorum longus muscle are compromised in 2- to 20-mo-old mdx mice. *J Appl Physiol (1985)*,
690 110(6), 1656-1663. doi:10.1152/jappphysiol.01425.2010

691 Huang, P., Cheng, G., Lu, H., Aronica, M., Ransohoff, R. M., & Zhou, L. (2011). Impaired respiratory
692 function in mdx and mdx/utrn(+/-) mice. *Muscle Nerve*, 43(2), 263-267. doi:10.1002/mus.21848

693 Huebner, K. D., Jassal, D. S., Halevy, O., Pines, M., & Anderson, J. E. (2008). Functional resolution of
694 fibrosis in mdx mouse dystrophic heart and skeletal muscle by halofuginone. *Am J Physiol Heart*
695 *Circ Physiol*, *294*(4), H1550-1561. doi:10.1152/ajpheart.01253.2007

696 Infante, A. S., Stein, M. S., Zhai, Y., Borisy, G. G., & Gundersen, G. G. (2000). Detyrosinated (Glu)
697 microtubules are stabilized by an ATP-sensitive plus-end cap. *J Cell Sci*, *113* (Pt 22), 3907-3919.

698 Ishizaki, M., Suga, T., Kimura, E., Shiota, T., Kawano, R., Uchida, Y., . . . Uchino, M. (2008). Mdx
699 respiratory impairment following fibrosis of the diaphragm. *Neuromuscul Disord*, *18*(4), 342-348.
700 doi:10.1016/j.nmd.2008.02.002

701 Iyer, S. R., Shah, S. B., Valencia, A. P., Schneider, M. F., Hernandez-Ochoa, E. O., Stains, J. P., . . . Lovering,
702 R. M. (2017). Altered nuclear dynamics in MDX myofibers. *J Appl Physiol* (1985), *122*(3), 470-481.
703 doi:10.1152/jappphysiol.00857.2016

704 Kennedy, B. F., Wijesinghe, P., & Sampson, D. D. (2017). The emergence of optical elastography in
705 biomedicine. *Nature Photonics*, *11*, 215. doi:10.1038/nphoton.2017.6

706 Kerr, J. P., Robison, P., Shi, G., Bogush, A. I., Kempema, A. M., Hexum, J. K., . . . Ward, C. W. (2015).
707 Detyrosinated microtubules modulate mechanotransduction in heart and skeletal muscle. *Nat*
708 *Commun*, *6*, 8526. doi:10.1038/ncomms9526

709 Khairallah, R. J., Shi, G., Sbrana, F., Prosser, B. L., Borroto, C., Mazaitis, M. J., . . . Ward, C. W. (2012).
710 Microtubules underlie dysfunction in duchenne muscular dystrophy. *Sci.Signal.*, *5*(236), ra56.
711 doi:10.1126/scisignal.2002829 [pii];10.1126/scisignal.2002829 [doi]

712 Khawaja, S., Gundersen, G. G., & Bulinski, J. C. (1988). Enhanced stability of microtubules enriched in
713 detyrosinated tubulin is not a direct function of detyrosination level. *J Cell Biol*, *106*(1), 141-149.

714 Krouskop, T. A., Wheeler, T. M., Kallel, F., Garra, B. S., & Hall, T. (1998). Elastic moduli of breast and
715 prostate tissues under compression. *Ultrason Imaging*, *20*(4), 260-274.
716 doi:10.1177/016173469802000403

717 Kumar, A., Khandelwal, N., Malya, R., Reid, M. B., & Boriek, A. M. (2004). Loss of dystrophin causes
718 aberrant mechanotransduction in skeletal muscle fibers. *FASEB J*, *18*(1), 102-113.
719 doi:10.1096/fj.03-0453com

720 Landino, L. M., Moynihan, K. L., Todd, J. V., & Kennett, K. L. (2004). Modulation of the redox state of
721 tubulin by the glutathione/glutaredoxin reductase system. *Biochemical and Biophysical Research*
722 *Communications*, *314*(2), 555-560. doi:<http://dx.doi.org/10.1016/j.bbrc.2003.12.126>

723 Lanza, G. A., Russo, A. D., Giglio, V., De Luca, L., Messano, L., Santini, C., . . . Bellocchi, F. (2001).
724 Impairment of cardiac autonomic function in patients with Duchenne muscular dystrophy:
725 Relationship to myocardial and respiratory function. *American Heart Journal*, *141*(5), 808-812.
726 doi:<http://dx.doi.org/10.1067/mhj.2001.114804>

727 Larin, K. V., & Sampson, D. D. (2017). Optical coherence elastography - OCT at work in tissue
728 biomechanics [Invited]. *Biomed Opt Express*, *8*(2), 1172-1202. doi:10.1364/BOE.8.001172

729 Levi, O., Genin, O., Angelini, C., Halevy, O., & Pines, M. (2015). Inhibition of muscle fibrosis results in
730 increases in both utrophin levels and the number of revertant myofibers in Duchenne muscular
731 dystrophy. *Oncotarget*, *6*(27), 23249-23260.

732 Li, C., Guan, G., Huang, Z., Johnstone, M., & Wang, R. K. (2012). Noncontact all-optical measurement of
733 corneal elasticity. *Opt Lett*, *37*(10), 1625-1627. doi:10.1364/OL.37.001625

734 Liu, W., & Ralston, E. (2014). A new directionality tool for assessing microtubule pattern alterations.
735 *Cytoskeleton (Hoboken)*, *71*(4), 230-240. doi:10.1002/cm.21166

736 Lopez, M. A., Pardo, P. S., Cox, G. A., & Boriek, A. M. (2008). Early mechanical dysfunction of the
737 diaphragm in the muscular dystrophy with myositis (Ttnmdm) model. *Am J Physiol Cell Physiol*,
738 *295*(5), C1092-1102. doi:10.1152/ajpcell.16.2008

739 Mathur, A. B., Collinsworth, A. M., Reichert, W. M., Kraus, W. E., & Truskey, G. A. (2001). Endothelial,
740 cardiac muscle and skeletal muscle exhibit different viscous and elastic properties as determined
741 by atomic force microscopy. *J Biomech*, *34*(12), 1545-1553.

742 Mead, A. F., Petrov, M., Malik, A. S., Mitchell, M. A., Childers, M. K., Bogan, J. R., . . . Stedman, H. H.
743 (2014). Diaphragm remodeling and compensatory respiratory mechanics in a canine model of

744 Duchenne muscular dystrophy. *Journal of Applied Physiology*, 116(7), 807-815.
745 doi:10.1152/jappphysiol.00833.2013

746 Mendez, J., & Keys, A. (1960). Density and composition of mammalian muscle. *Metabolism*, 9, 184-188.

747 Meyer, G. A., & Lieber, R. L. (2011). Elucidation of extracellular matrix mechanics from muscle fibers and
748 fiber bundles. *J Biomech*, 44(4), 771-773. doi:10.1016/j.jbiomech.2010.10.044

749 Mobley, B. A., & Eisenberg, B. R. (1975). Sizes of components in frog skeletal muscle measured by
750 methods of stereology. *J Gen Physiol*, 66(1), 31-45.

751 Morris, E. J., Nader, G. P., Ramalingam, N., Bartolini, F., & Gundersen, G. G. (2014). Kif4 interacts with
752 EB1 and stabilizes microtubules downstream of Rho-mDia in migrating fibroblasts. *PLoS ONE*,
753 9(3), e91568. doi:10.1371/journal.pone.0091568

754 Myers, K. A., Applegate, K. T., Danuser, G., Fischer, R. S., & Waterman, C. M. (2011). Distinct ECM
755 mechanosensing pathways regulate microtubule dynamics to control endothelial cell branching
756 morphogenesis. *The Journal of Cell Biology*, 192(2), 321-334. doi:10.1083/jcb.201006009

757 Oberai, A. A., Gokhale, N. H., Goenezen, S., Barbone, P. E., Hall, T. J., Sommer, A. M., & Jiang, J. (2009).
758 Linear and nonlinear elasticity imaging of soft tissue in vivo: demonstration of feasibility. *Phys
759 Med Biol*, 54(5), 1191-1207. doi:10.1088/0031-9155/54/5/006

760 Pal, R., Palmieri, M., Loehr, J. A., Li, S., Abo-Zahrah, R., Monroe, T. O., . . . Rodney, G. G. (2014). Src-
761 dependent impairment of autophagy by oxidative stress in a mouse model of Duchenne
762 muscular dystrophy. *Nat Commun*, 5, 4425. doi:10.1038/ncomms5425

763 Passerieux, E., Rossignol, R., Letellier, T., & Delage, J. P. (2007). Physical continuity of the perimysium
764 from myofibers to tendons: involvement in lateral force transmission in skeletal muscle. *J Struct
765 Biol*, 159(1), 19-28. doi:10.1016/j.jsb.2007.01.022

766 Patel, T. J., & Lieber, R. L. (1997). Force transmission in skeletal muscle: from actomyosin to external
767 tendons. *Exerc Sport Sci Rev*, 25, 321-363.

768 Pavan, T. Z., Madsen, E. L., Frank, G. R., Adilton, O. C. A., & Hall, T. J. (2010). Nonlinear elastic behavior of
769 phantom materials for elastography. *Phys Med Biol*, 55(9), 2679-2692. doi:10.1088/0031-
770 9155/55/9/017

771 Peachey, L. D. (1965). The sarcoplasmic reticulum and transverse tubules of the frog's sartorius. *J Cell
772 Biol*, 25(3), Suppl:209-231.

773 Percival, J. M., Gregorevic, P., Odom, G. L., Banks, G. B., Chamberlain, J. S., & Froehner, S. C. (2007).
774 rAAV6-microdystrophin rescues aberrant Golgi complex organization in mdx skeletal muscles.
775 *Traffic*, 8(10), 1424-1439. doi:10.1111/j.1600-0854.2007.00622.x

776 Percival, J. M., Whitehead, N. P., Adams, M. E., Adamo, C. M., Beavo, J. A., & Froehner, S. C. (2012).
777 Sildenafil reduces respiratory muscle weakness and fibrosis in the mdx mouse model of
778 Duchenne muscular dystrophy. *J Pathol*, 228(1), 77-87. doi:10.1002/path.4054

779 Pessina, P., Kharraz, Y., Jardi, M., Fukada, S., Serrano, A. L., Perdiguero, E., & Munoz-Canoves, P. (2015).
780 Fibrogenic Cell Plasticity Blunts Tissue Regeneration and Aggravates Muscular Dystrophy. *Stem
781 Cell Reports*, 4(6), 1046-1060. doi:10.1016/j.stemcr.2015.04.007

782 Prins, K. W., Humston, J. L., Mehta, A., Tate, V., Ralston, E., & Ervasti, J. M. (2009). Dystrophin is a
783 microtubule-associated protein. *The Journal of Cell Biology*, 186(3), 363-369.
784 doi:10.1083/jcb.200905048

785 Purslow, P. P., & Trotter, J. A. (1994). The morphology and mechanical properties of endomysium in
786 series-fibred muscles: variations with muscle length. *J Muscle Res Cell Motil*, 15(3), 299-308.

787 Putnam, A. J., Cunningham, J. J., Pillemer, B. B. L., & Mooney, D. J. (2003). *External mechanical strain
788 regulates membrane targeting of Rho GTPases by controlling microtubule assembly* (Vol. 284).

789 Putnam, A. J., Schultz, K., & Mooney, D. J. (2001). Control of microtubule assembly by extracellular
790 matrix and externally applied strain. *Am J Physiol Cell Physiol*, 280(3), C556-564.

791 Ralston, E., Lu, Z., & Ploug, T. (1999). The organization of the Golgi complex and microtubules in skeletal
792 muscle is fiber type-dependent. *J Neurosci*, 19(24), 10694-10705.

793 Ralston, E., Ploug, T., Kalthovde, J., & Lømo, T. (2001). Golgi Complex, Endoplasmic Reticulum Exit Sites,
794 and Microtubules in Skeletal Muscle Fibers Are Organized by Patterned Activity. *The Journal of*
795 *Neuroscience*, 21(3), 875-883.

796 Ramaswamy, K. S., Palmer, M. L., van der Meulen, J. H., Renoux, A., Kostrominova, T. Y., Michele, D. E., &
797 Faulkner, J. A. (2011). Lateral transmission of force is impaired in skeletal muscles of dystrophic
798 mice and very old rats. *The Journal of Physiology*, 589(Pt 5), 1195-1208.
799 doi:10.1113/jphysiol.2010.201921

800 Roberts, N. W., Holley-Cuthrell, J., Gonzalez-Vega, M., Mull, A. J., & Heydemann, A. (2015). Biochemical
801 and Functional Comparisons of mdx and Sgcg(-/-) Muscular Dystrophy Mouse Models. *Biomed*
802 *Res Int*, 2015, 131436. doi:10.1155/2015/131436

803 Robison, P., Caporizzo, M. A., Ahmadzadeh, H., Bogush, A. I., Chen, C. Y., Margulies, K. B., . . . Prosser, B.
804 L. (2016). Detyrosinated microtubules buckle and bear load in contracting cardiomyocytes.
805 *Science*, 352(6284), aaf0659. doi:10.1126/science.aaf0659

806 Rowe, J., Chen, Q., Domire, Z. J., McCullough, M. B., Sieck, G., Zhan, W. Z., & An, K. N. (2010). Effect of
807 collagen digestion on the passive elastic properties of diaphragm muscle in rat. *Med Eng Phys*,
808 32(1), 90-94. doi:10.1016/j.medengphy.2009.11.002

809 Skoufias, D. A., & Wilson, L. (1998). Assembly and colchicine binding characteristics of tubulin with
810 maximally tyrosinated and detyrosinated alpha-tubulins. *Arch Biochem Biophys*, 351(1), 115-
811 122. doi:10.1006/abbi.1997.0510

812 Smith, L. R., & Barton, E. R. (2014). Collagen content does not alter the passive mechanical properties of
813 fibrotic skeletal muscle in mdx mice. *Am J Physiol Cell Physiol*, 306(10), C889-898.
814 doi:10.1152/ajpcell.00383.2013

815 Stedman, H. H., Sweeney, H. L., Shrager, J. B., Maguire, H. C., Panettieri, R. A., Petrof, B., . . . Kelly, A. M.
816 (1991). The mdx mouse diaphragm reproduces the degenerative changes of Duchenne muscular
817 dystrophy. *Nature*, 352(6335), 536-539. doi:10.1038/352536a0

818 Trotter, J. A., & Purslow, P. P. (1992). Functional morphology of the endomysium in series fibered
819 muscles. *J Morphol*, 212(2), 109-122. doi:10.1002/jmor.1052120203

820 Turgeman, T., Hagai, Y., Huebner, K., Jassal, D. S., Anderson, J. E., Genin, O., . . . Pines, M. (2008).
821 Prevention of muscle fibrosis and improvement in muscle performance in the mdx mouse by
822 halofuginone. *Neuromuscul Disord*, 18(11), 857-868. doi:10.1016/j.nmd.2008.06.386

823 van Zwieten, R. W., Puttini, S., Lekka, M., Witz, G., Gicquel-Zouida, E., Richard, I., . . . Mermod, N. (2013).
824 Assessing dystrophies and other muscle diseases at the nanometer scale by atomic force
825 microscopy. *Nanomedicine*, 9(4), 393-406. doi:10.2217/nnm.12.215

826 Veronda, D. R., & Westmann, R. A. (1970). Mechanical characterization of skin-finite deformations. *J*
827 *Biomech*, 3(1), 111-124.

828 Virgilio, K. M., Martin, K. S., Peirce, S. M., & Blemker, S. S. (2015). Multiscale models of skeletal muscle
829 reveal the complex effects of muscular dystrophy on tissue mechanics and damage
830 susceptibility. *Interface Focus*, 5(2), 20140080. doi:10.1098/rsfs.2014.0080

831 Wang, S., & Larin, K. V. (2014). Shear wave imaging optical coherence tomography (SWI-OCT) for ocular
832 tissue biomechanics. *Optics Letters*, 39(1), 41-44.

833 Wang, S., Larin, K. V., Li, J., Vantipalli, S., Manapuram, R. K., Aglyamov, S., . . . Twa, M. D. (2013). A
834 focused air-pulse system for optical-coherence-tomography-based measurements of tissue
835 elasticity. *Laser Physics Letters*, 10(7), 075605.

836 Wang, S., Li, J., Manapuram, R. K., Menodiado, F. M., Ingram, D. R., Twa, M. D., . . . Larin, K. V. (2012).
837 Noncontact measurement of elasticity for the detection of soft-tissue tumors using phase-
838 sensitive optical coherence tomography combined with a focused air-puff system. *Optics*
839 *Letters*, 37(24), 5184-5186. doi:10.1364/OL.37.005184

840 Wang, S., Lopez, A. L., Morikawa, Y., Tao, G., Li, J., Larina, I. V., . . . Larin, K. V. (2014). Noncontact
841 quantitative biomechanical characterization of cardiac muscle using shear wave imaging optical
842 coherence tomography. *Biomedical Optics Express*, 5(7), 1980-1992. doi:10.1364/BOE.5.001980

- 843 Webster, D. R., Wehland, J., Weber, K., & Borisy, G. G. (1990). Detyrosination of alpha tubulin does not
844 stabilize microtubules in vivo. *J Cell Biol*, 111(1), 113-122.
- 845 Whitehead, N. P., Kim, M. J., Bible, K. L., Adams, M. E., & Froehner, S. C. (2015a). A new therapeutic
846 effect of simvastatin revealed by functional improvement in muscular dystrophy. *Proc Natl Acad*
847 *Sci U S A*. doi:10.1073/pnas.1509536112
- 848 Whitehead, N. P., Yeung, E. W., Froehner, S. C., & Allen, D. G. (2010). Skeletal muscle NADPH oxidase is
849 increased and triggers stretch-induced damage in the mdx mouse. *PLoS.One.*, 5(12), e15354.
850 doi:10.1371/journal.pone.0015354 [doi]
- 851 Wilson, C., & Gonzalez-Billault, C. (2015). Regulation of cytoskeletal dynamics by redox signaling and
852 oxidative stress: implications for neuronal development and trafficking. *Front Cell Neurosci*, 9,
853 381. doi:10.3389/fncel.2015.00381
- 854 Wolff, A. V., Niday, A. K., Voelker, K. A., Call, J. A., Evans, N. P., Granata, K. P., & Grange, R. W. (2006).
855 Passive mechanical properties of maturing extensor digitorum longus are not affected by lack of
856 dystrophin. *Muscle & Nerve*, 34(3), 304-312. doi:10.1002/mus.20588
- 857 Wood, L. K., Kayupov, E., Gumucio, J. P., Mendias, C. L., Clafin, D. R., & Brooks, S. V. (2014). Intrinsic
858 stiffness of extracellular matrix increases with age in skeletal muscles of mice. *Journal of Applied*
859 *Physiology*, 117(4), 363-369. doi:10.1152/jappphysiol.00256.2014

860

861 **Table 1. Tubulin and stiffness correlations**

Adj R ²	Fibrosis	α - tubulin	β - tubulin	DT- tubulin	DT-/ α - tubulin	MLR (fibrosis/glu)	MLR (fibrosis/ratio)
Transverse	0.69 *	0.46 *	0.51 *	0.51 *	0.10	0.69	0.67
Longitudinal	0.44 *	0.20 *	0.40 *	0.41 *	0.19 *	0.44	0.49

862
863

864 Most variables significantly correlated with both transverse and longitudinal stiffness. MLR
865 revealed fibrosis accounted for the majority of the variance observed in either stiffness measure.
866 $p \leq 0.05$ *Significant correlation in at least $n_{\text{animals}}=6$.

867

868

869 **Table 2. Force and stiffness correlations**

Adj R ²	Fibrosis	MLR (fibrosis/trans)	MLR (fibrosis/long)	MLR (fibrosis/long/trans)
Force	0.57	0.52	0.52	0.49

870

871 MLR revealed fibrosis accounted for a majority of the variance observed in diaphragm muscle
872 function. $p \leq 0.05$ *Significant difference between groups in at least $n_{\text{animals}}=6$.

873

874

875

876 **Table 3. Respiratory function**

	WT	<i>mdx</i>	<i>p47^(-/-)/mdx</i>
f (breath/min)	408.2 ± 14.5 *	279.8 ± 18.3	377.3 ± 17.0 *
T _v (ml)	0.25 ± .009	0.24 ± .008	0.26 ± .012
M _v (ml)	100.3 ± 5.6 *	65.9 ± 17.6	99.2 ± 8.6 *
PIF (ml/s)	7.6 ± 0.30 *	5.9 ± 0.56	8.0 ± 0.51 *
PEF (ml/s)	4.2 ± 0.25	3.2 ± 0.24	4.4 ± 0.39 *
T _i (s)	0.057 ± .002 *	0.080 ± .007	0.057 ± .002 *
T _e (s)	0.129 ± .009 *	0.190 ± .012	0.138 ± .008 *

877

878 Dystrophic mice lacking Nox 2 ROS production maintained respiratory function similar to WT
879 levels. $p \leq 0.05$ *Significant difference vs. *mdx* in at least $n_{\text{animals}}=9$.

880

881

882 **Figure 1. Eliminating Nox 2 ROS production prevents alterations in tubulin content and**
883 **the microtubule network.** **A.** Representative western blot images of α -, β -, and DT-tubulin
884 content in all three genotypes. **B-D.** Eliminating Nox2 ROS production decreases absolute α -, β -
885 and DT-tubulin content in dystrophic diaphragm muscle. **E.** The relative amount of DT-/ α -
886 tubulin is not different between groups. **F.** Representative images of diaphragm myofibers
887 stained with α -tubulin. **G-I.** The lack of Nox 2 ROS prevents microtubule disorganization and
888 the increase in microtubule density seen in *mdx* muscle. $p \leq 0.05$ *Significant difference between
889 groups in at least (A-E) $n_{\text{animals}} = 6$ and (F-I) $n_{\text{animals}} = 3$ and $n_{\text{fibers}} = 15$.

890

891 **Figure 2. Genetic deletion of Nox2 ROS production reduced fibrosis.**

892 **A.** Representative trichrome images of fibrosis in all three genotypes. Eliminating Nox2 ROS
893 production in dystrophic muscle reduced fibrosis compared with *mdx* mice. **B.** Hydroxyproline
894 levels were elevated in dystrophic muscle and eliminating Nox2 ROS reduced hydroxyproline
895 content compared with *mdx* mice. **C.** Representative western blot images for fibronectin and
896 collagen I content in all three genotypes. Fibronectin and collagen I content were elevated in *mdx*
897 diaphragm and eliminating Nox2 ROS reduced both toward WT levels. $p \leq 0.05$ * Significant
898 difference between groups in at least $n_{\text{animals}} = 6$ for trichrome and hydroxyproline and $n_{\text{animals}} = 3$
899 for fibronectin and collagen I.

900

901 **Figure 3. The lack of Nox2 ROS reduces muscle stiffness and stretch induced ROS.**

902 **A.** Image of the passive stretch experimental set-up. **B.** Average passive diaphragm force
903 recorded during stretch for each genotype. **C.** Eliminating Nox2 ROS production reduced
904 diaphragm tissue stiffness. **D.** Stretch induced ROS in *mdx* muscle was elevated above WT levels
905 and eliminated in *p47^{-/-}/mdx* diaphragm. **E.** Image of the OCE experimental set-up. **F.**
906 Representative OCT image of the diaphragm taken prior to OCE experiments. **G.** Transverse
907 diaphragm muscle stiffness increased in *mdx* compared with WT mice; eliminating Nox2 ROS
908 resulted in a decrease toward WT ($p = 0.09$). **H.** Genetic inhibition of Nox2 ROS reduced
909 longitudinal diaphragm stiffness to WT values. **I.** Muscle function was not altered following
910 OCE measurements. $p \leq 0.05$ *Significant difference between groups in at least $n_{\text{animals}} = 6$ per
911 group.

912

913

914 **Figure 4. Eliminating Nox2 ROS protects against muscle and respiratory dysfunction.**

915 **A.** WT was significantly different from *mdx* and *p47^{-/-}/mdx* animals at all stimulation
916 frequencies. The *p47^{-/-}/mdx* animals were different from *mdx* at 60-100 Hz and trended towards
917 significance at 40 Hz ($p = 0.098$). **B.** Fibrosis significantly correlated with muscle force. $p \leq 0.05$
918 *Significant difference between groups in at least $n_{\text{animals}} = 6$.

919

920 **Figure 5. Taxol induced MT polymerization has no effect on tissue stiffness but induced**
921 **ROS production.** **A.** Representative images of MT network in control (DMSO) and Taxol
922 treated diaphragm (20 μM for 2 hr). **B-D.** Taxol induced MT disorganization and increased
923 microtubule density compared with control. **E.** Average passive diaphragm force recorded
924 during stretch was not affected by Taxol. **F.** Polymerizing the MT network had no effect on
925 diaphragm tissue stiffness. **G.** MT network polymerization enhanced stretch induced ROS in
926 Taxol treated diaphragm. $p \leq 0.05$ *Significant difference between groups in at least (A-D)

927 $n_{\text{animals}} = 3$ and $n_{\text{fibers}} = 15$ and (E-G) $n_{\text{animals}} = 5$.

928

929 **Supplemental Figure Legends**

930

931

932 **Figure 3- video 1**

933 Longitudinal. Following the application of the air puff (<1 ms in duration), the displacement of
934 the diaphragm tissue was monitored as the wave propagated down longitudinal axis while
935 imaged at 62.5 kHz with OCE. Visualization is 5000 times slower than the actual speed.

936

937 **Figure 4-figure supplement 1 Eliminating Nox2 ROS protects against phenotypic**
938 **alterations in dystrophic diaphragm muscle.**

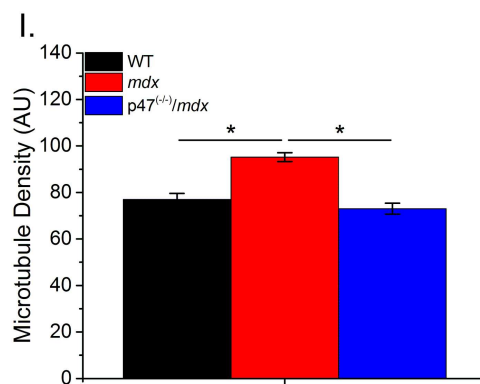
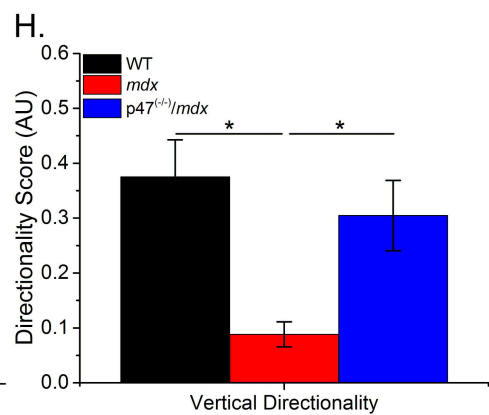
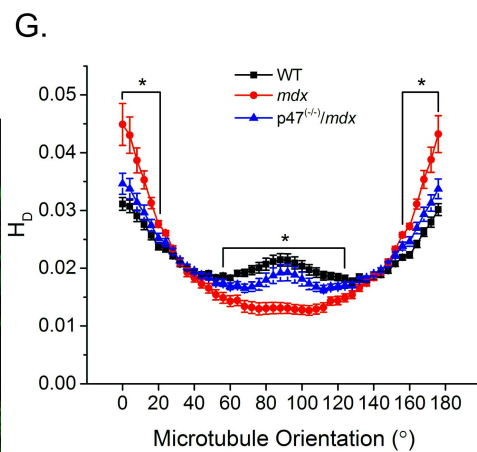
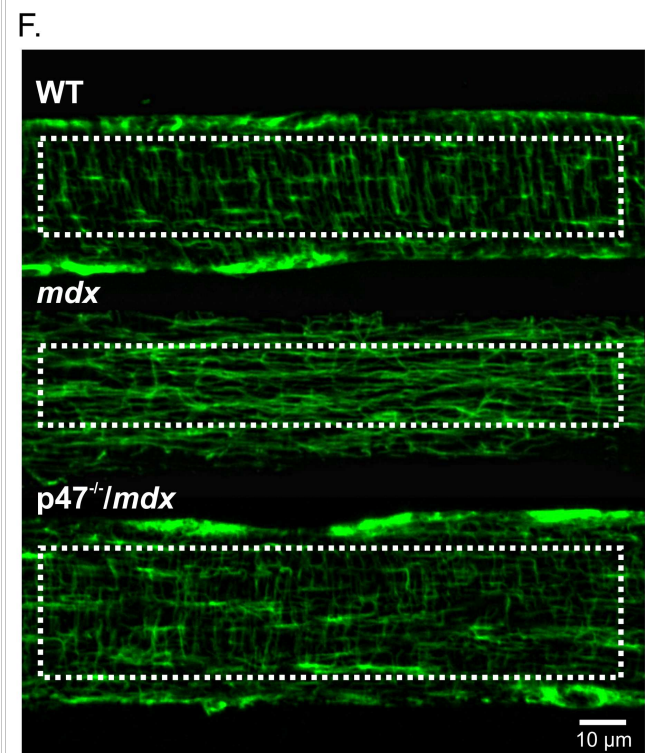
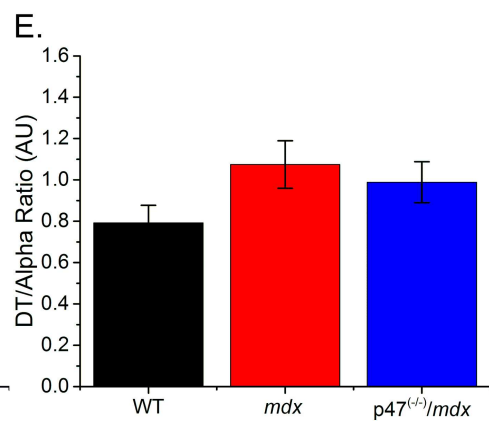
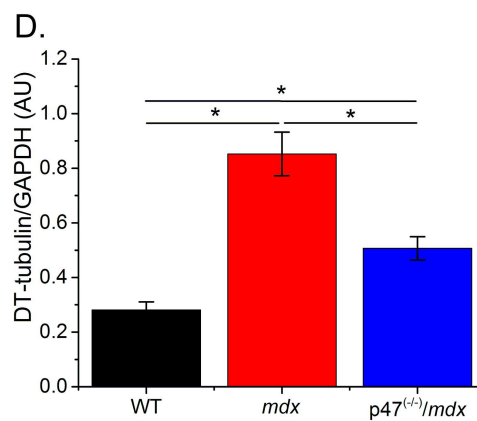
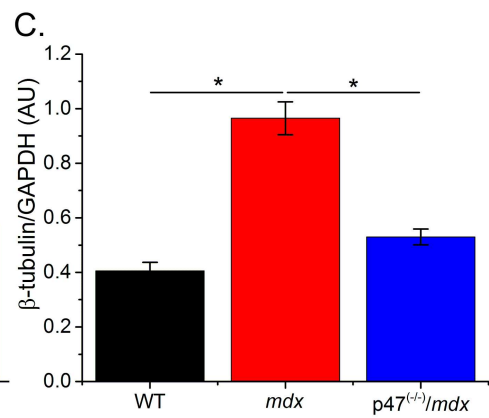
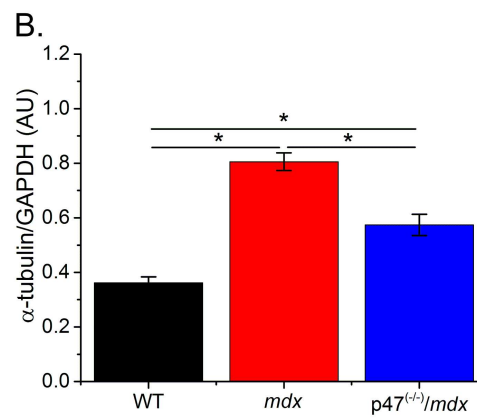
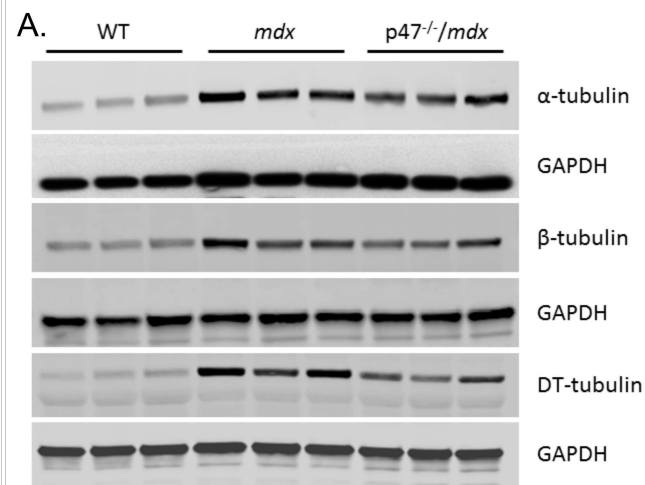
939 **A-B.** Eliminating Nox2 ROS increased median cross sectional area compared with *mdx*
940 diaphragm. **C.** In dystrophic diaphragm lacking Nox2 ROS production the number of centralized
941 nuclei were reduced compared with *mdx* diaphragm tissue. **D.** Representative hematoxylin and
942 eosin stained images of diaphragm cross-section showing central nuclei (arrow head) and smaller
943 fibers (arrow). **E.** Fiber type distribution was maintained by eliminating Nox2 ROS production in
944 dystrophic diaphragm muscle. **F.** Representative immunofluorescently labeled diaphragm cross-
945 sectional images showing fiber type distribution. Type I (red), IIA (green), IIB/IIX (white x,
946 unstained and viewed from bright field overlay). $p \leq 0.05$ *Significant difference between groups
947 in at least $n_{\text{animals}}=3$.

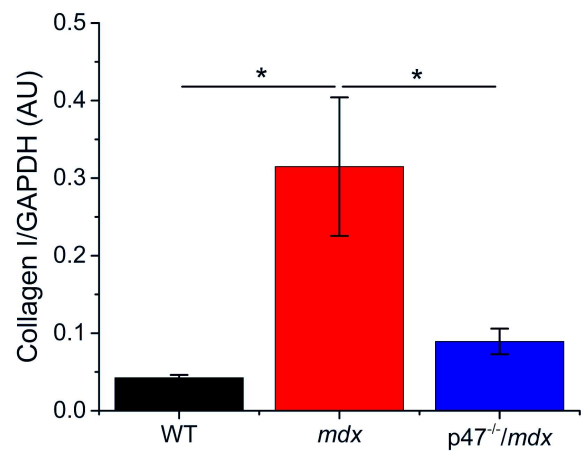
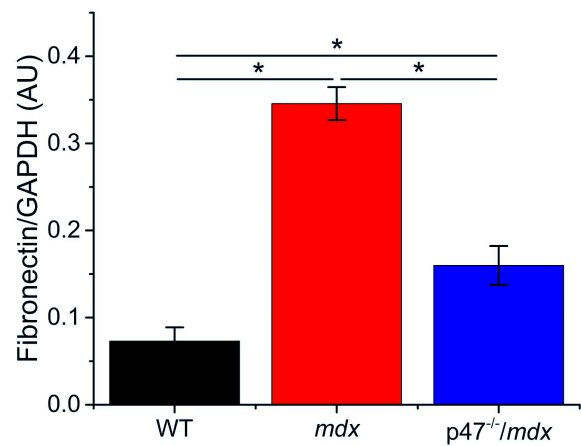
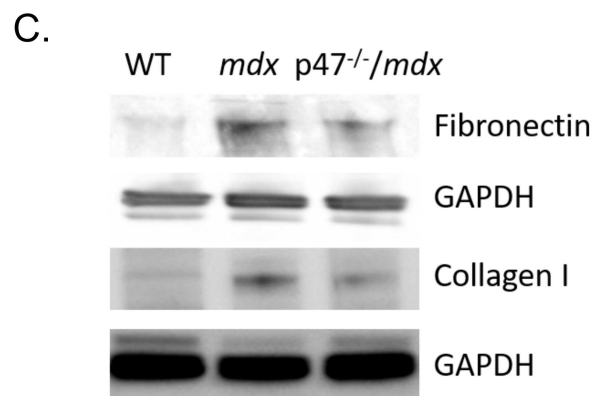
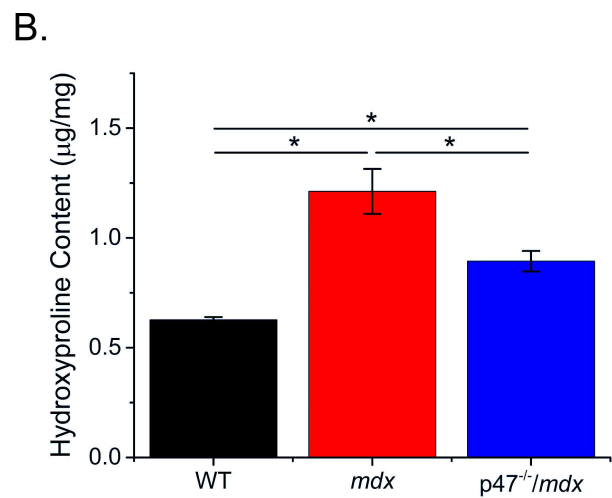
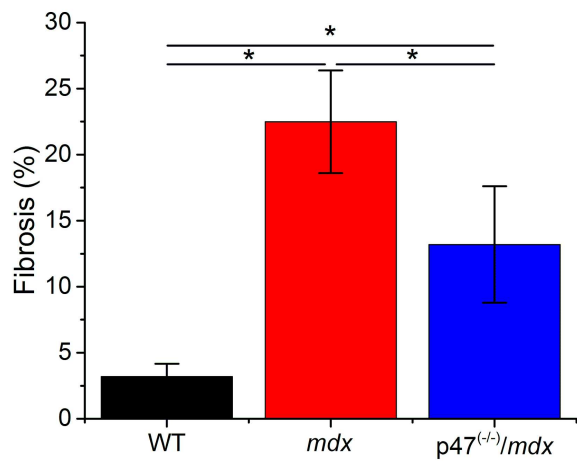
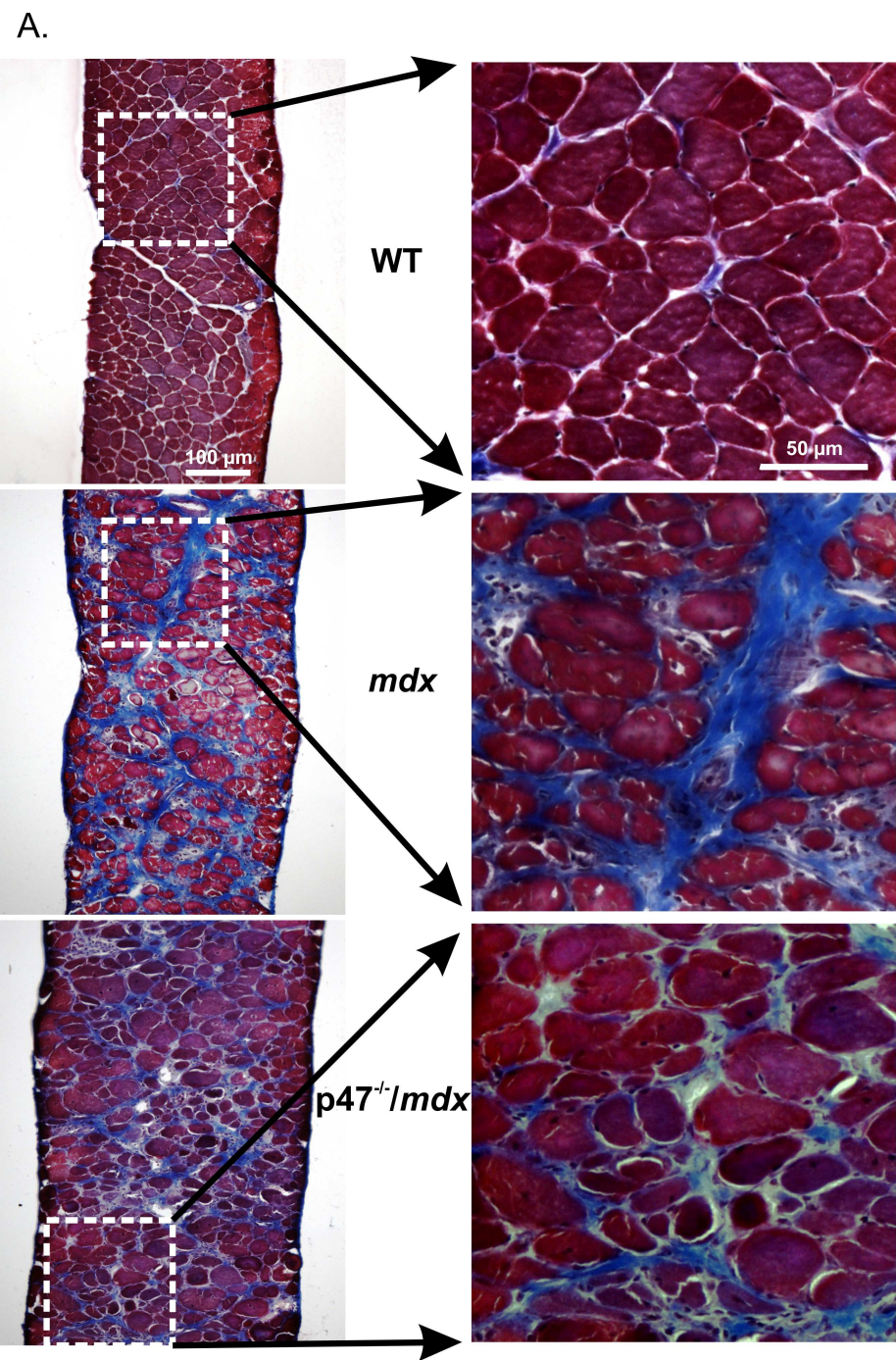
948

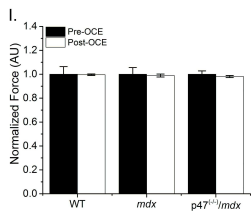
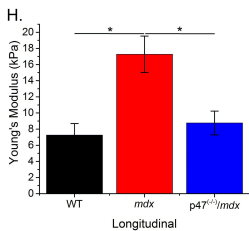
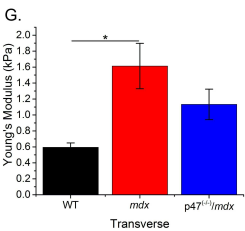
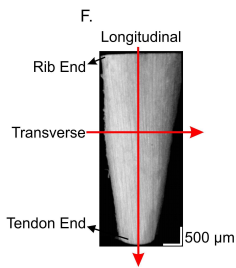
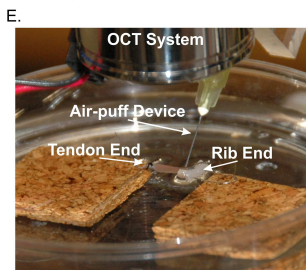
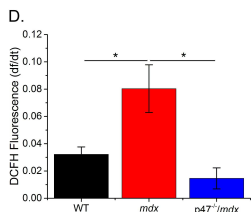
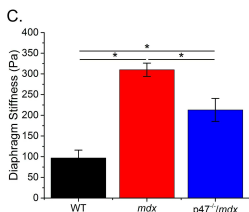
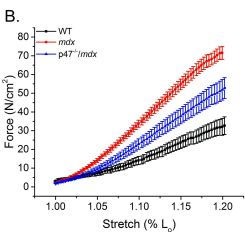
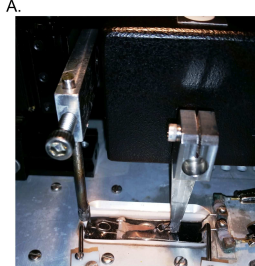
949 **Figure 4-figure supplement 2 Linear correlation of stiffness measured by OCE and the**
950 **peak force**

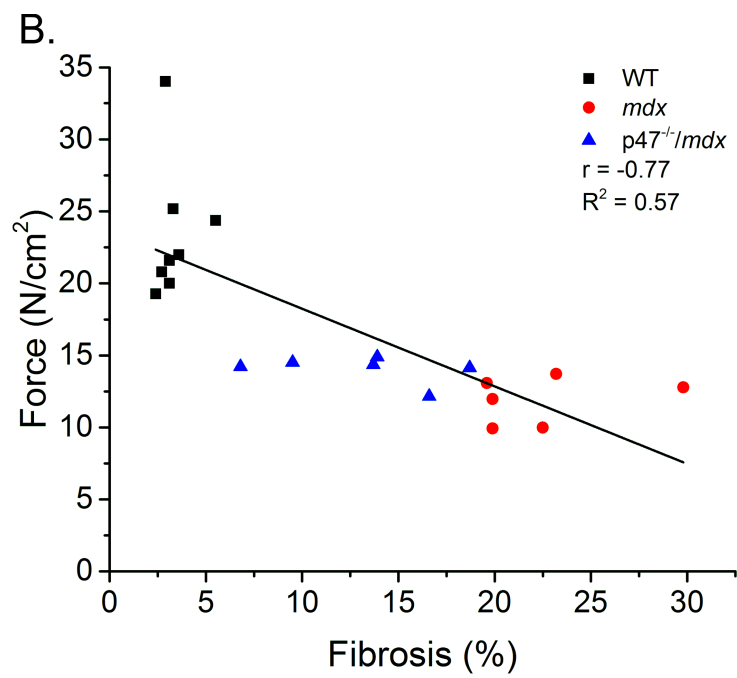
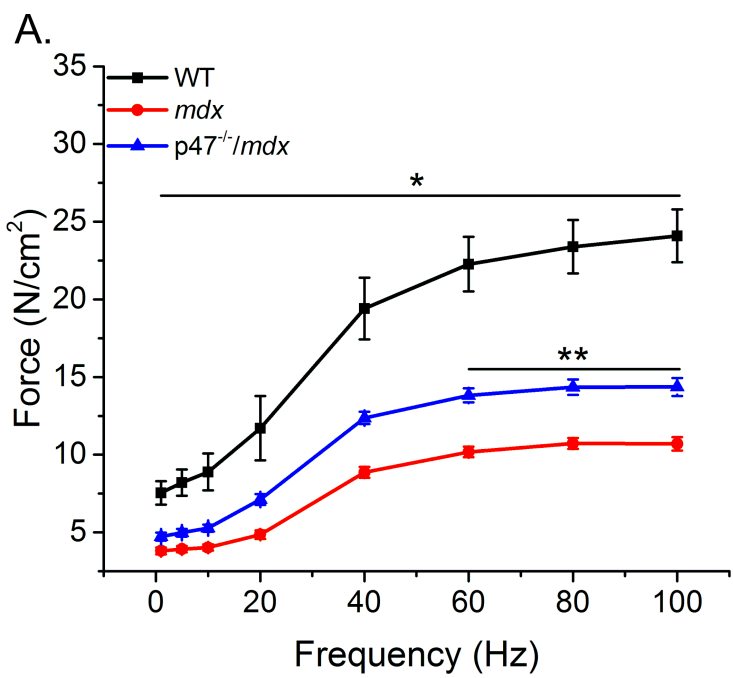
951 There was a significant correlation between peak force and transverse as well as peak force and
952 longitudinal diaphragm stiffness.

953









A.

